

ARTICLE

Open Access

Dean migration mechanisms: facilitating the control of microbial contaminants in cell therapy product manufacturing

Junhao Tan^{1,2}, Jianbo Yang², Junjie Huang², Ziming Huang², Liang Xu², Weizhao Yao^{1,2}, Chengshun Shen^{1,2}, Ming Zhao²✉ and Luping Zhou²✉

Abstract

Cell therapy products are rapidly transforming clinical practice, but their short shelf-lives and inability to undergo terminal sterilization create major challenges for sterility testing. Conventional rapid microbiological methods (RMMs) are hindered by the dense cellular background of therapeutic samples, which masks rare microbial contaminants and necessitates pre-analytical processing. Efficient separation of microorganisms from high-density cell suspensions is therefore a critical prerequisite for enabling real-time, in-process sterility assurance. Here, we systematically elucidate the Dean flow-dominated migration mechanism and determine its effective range for continuous, label-free separation of non-typical contaminants $\leq 5 \mu\text{m}$ in microchannels exceeding $40 \mu\text{m}$ in height. We demonstrate that particles with $ap/h < 0.05$ undergo exclusive Dean-induced lateral migration, while those near the inertial focusing threshold ($ap/h \approx 0.07$) exhibit a Reynolds number-dependent transition between unfocused and centerline-focused streams. Leveraging these principles, we designed optimized channel geometries that achieved $> 95\%$ separation efficiency and $> 96\%$ purity of T cells versus three morphologically distinct bacteria at 10^5 bacteria/mL. At ultra-low loads (< 10 CFU/mL), culture-based assays confirmed 100% detection for inocula > 1 CFU/mL. Our findings validate Dean migration as a governing mechanism for submicron particle separation and provide a path toward integrating microfluidic modules into closed CAR-T manufacturing platforms, advancing real-time microbial quality control in cell therapy production.

Introduction

Cellular therapy products represent a transformative class of medicines, offering novel therapeutic avenues for diseases where conventional treatments have limited efficacy^{1,2}. However, their unique characteristics—including short shelf-lives, parenteral administration routes, and the inability to undergo terminal sterilization—present formidable challenges for microbial safety validation³. Traditional compendial sterility assays, as specified in USP < 71 >, require incubation periods of up

to 14 days and are thus inherently misaligned with the accelerated release timelines of most cell-based therapies. Due to this temporal disconnect, manufacturers often rely on validated in-process controls and comprehensive risk assessments to facilitate product release, while final sterility confirmation is typically obtained retrospectively⁴.

In response, global regulatory bodies, including the FDA and EMA, have encouraged the adoption of validated Rapid Microbiological Methods (RMMs), provided they demonstrate performance equivalent or superior to standard pharmacopeial methods^{5,6}. Despite this, the direct application of RMMs to cell therapy products is frequently hindered by the inherent complexity of the sample matrix and the low abundance of potential contaminants. The high density of therapeutic cells, such as T cells, interferes with detection, compelling the use of

Correspondence: Ming Zhao (Zmingys@ucas.ac.cn) or Luping Zhou (zhouluping6060@163.com)

¹Medical School, Faculty of Medicine, Tianjin University, Tianjin, China

²Hangzhou Institute of Medicine, Chinese Academy of Sciences, Hangzhou, Zhejiang, China

© The Author(s) 2026



Open Access This article is licensed under a Creative Commons Attribution-NonCommercial-NoDerivatives 4.0 International License, which permits any non-commercial use, sharing, distribution and reproduction in any medium or format, as long as you give appropriate credit to the original author(s) and the source, provide a link to the Creative Commons licence, and indicate if you modified the licensed material. You do not have permission under this licence to share adapted material derived from this article or parts of it. The images or other third party material in this article are included in the article's Creative Commons licence, unless indicated otherwise in a credit line to the material. If material is not included in the article's Creative Commons licence and your intended use is not permitted by statutory regulation or exceeds the permitted use, you will need to obtain permission directly from the copyright holder. To view a copy of this licence, visit <http://creativecommons.org/licenses/by-nc-nd/4.0/>.

pre-analytical sample processing steps like centrifugation, cell lysis, or filtration. For instance, growth-based RMMs (e.g., BACT/ALERT, BACTEC™) require the removal of viable eukaryotic cells to prevent false positives from metabolic activity, while membrane-based assays that rely on ATP bioluminescence or fluorescence (e.g., Milliflex Rapid System) necessitate cell removal to avoid signal masking and membrane fouling⁷. Although these technologies significantly reduce the time-to-result to ~5–7 days, they are not yet rapid enough to enable the real-time process control and supply chain feedback that the field urgently needs⁸. Even emerging microfluidic platforms for bacterial detection, such as digital and droplet microfluidics, which offer substantial gains in speed, are still constrained by cellular interference⁹. Consequently, the development of an efficient technology to separate target microorganisms from a high-density cellular background remains a critical bottleneck for advancing sterility testing in cell therapy⁸.

This challenge is further magnified within the Quality by Design (QbD) manufacturing paradigm, which strives to ensure product consistency through the real-time measurement of Critical Quality Attributes (CQAs)^{8,10}. While integrated “GMP-in-a-box” platforms have automated key manufacturing steps like cell selection, activation, and expansion, quality monitoring largely remains a disconnected, offline process. Samples are typically drawn from the bioreactor and transferred to a separate analytics laboratory, introducing risks of contamination and incurring significant delays that undermine the principle of immediate quality verification. To align with the goals of QbD and meet the demands for instantaneous logistical feedback, the development of technologies capable of continuous, on-line sample processing and analysis is paramount¹¹.

Inertial microfluidic technology is a label-free, passive sorting method that manipulates and separates particles or cells through the interaction between inertial forces and channel walls in microscale flow channels¹². This technique has been widely applied to the separation of large particles (5–20 μm)^{13,14}, such as red blood cells¹³, white blood cells¹⁵, and circulating tumor cells (CTCs)¹⁶. However, studies on nanoscale and submicron particles ($\leq 5 \mu\text{m}$) remain relatively limited. According to the principle of inertial focus ($a_p/h \geq 0.07$)^{17,18}, as the particle size decreases, the required channel height also decreases ($\leq 35 \mu\text{m}$). However, lower channel heights increase the risk of clogging and reactor failure, requiring that the maximum particle diameter in the sample be $\leq 0.5h$. Dean flow fractionation (DFF)^{19,20} leverages Dean secondary flow to induce controlled migration of small particles (e.g., bacteria, nanoparticles, and biomolecules) toward the outer channel wall, while larger target cells remain inertially focused near the inner wall, enabling efficient

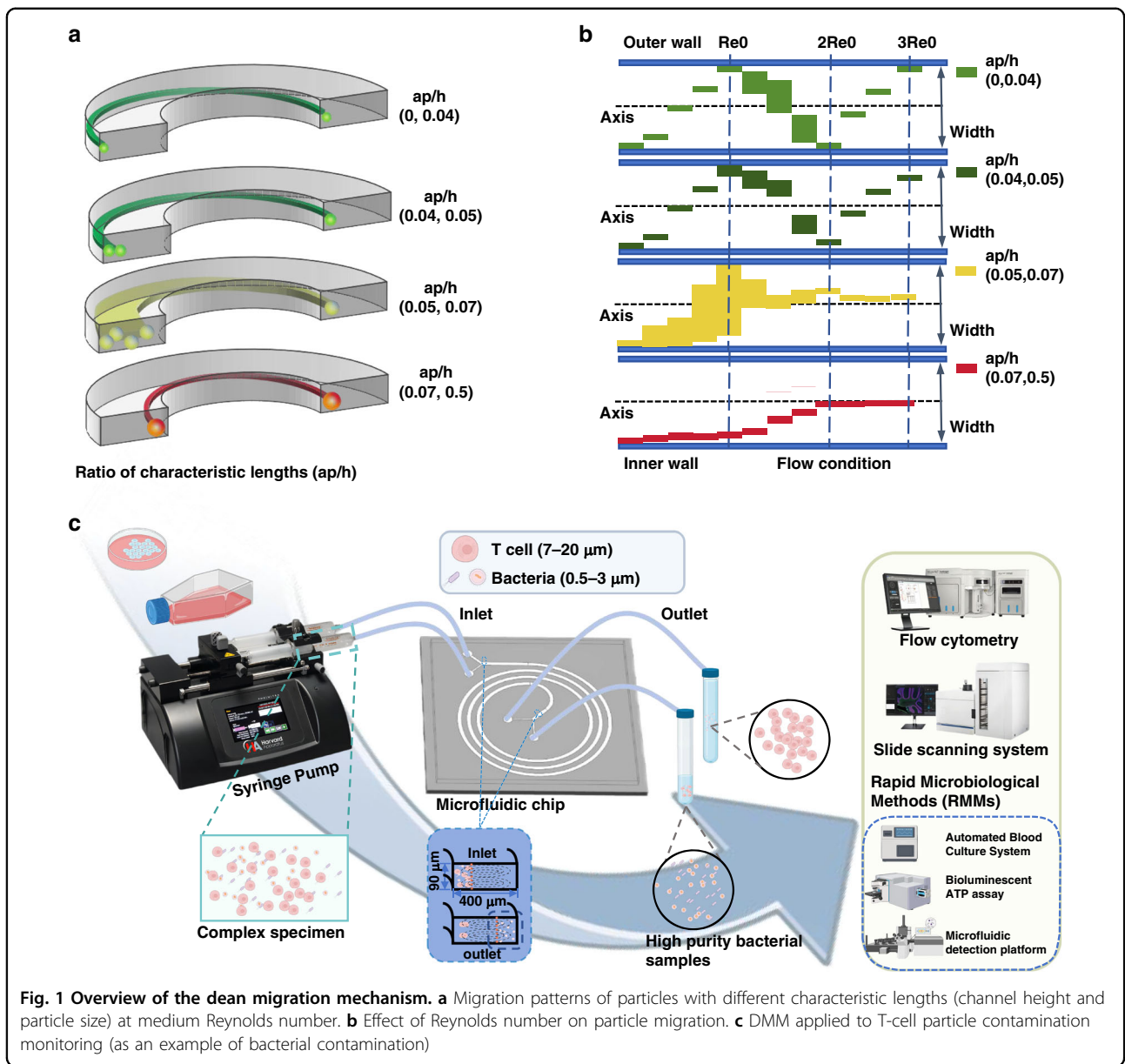
separation. Previous studies have demonstrated that a high sheath-to-sample flow ratio is essential for separation methods based on Dean migration²¹. Other studies have further advanced the development of Dean migration-based separation methods^{22–26}. However, the conditions under which Dean migration occurs remain unclear, lacking theoretical or experimental evidence similar to the inertial migration principle ($a_p/h \geq 0.07$). The current understanding is merely summarized as Dean-induced migration occurring when $a_p/h < 0.07$. Moreover, most experimental samples used in existing studies do not involve complex biological samples, leaving room for improvement in separation efficiency.

In this study, we focus on non-typical particulate contaminants ($a_p \leq 5 \mu\text{m}$), which commonly arise in cell-culture bioreactors, and their lateral focusing and migration in microchannels with heights exceeding 40 μm . We demonstrate for the first time that, at moderate Reynolds numbers, particles satisfying $a_p/h < 0.05$ are exclusively governed by Dean-induced lateral migration (Fig. 1a), whereas at low Reynolds numbers this Dean-dominant regime extends to $a_p/h < 0.06$. Particles with a_p/h close to 0.07 exhibit a Re-dependent transition from unfocused streams to focused streams near the channel centerline (Fig. 1b). Leveraging these insights, we optimized channel geometry and flow conditions to achieve efficient separation of T-cells from contaminant particles. Validation experiments at moderate Re using three morphologically distinct bacteria confirmed that Dean drag drives bacterial focusing into a tight stream along the outer wall, while inertial lift forces focus T-cells near the inner wall (Fig. 1c). Flow cytometry and microscopy counts at high contamination loads (10^5 CFU/mL) yielded $> 95\%$ separation efficiency and $> 96\%$ purity. Membrane-based culture assays at ultra-low loads (< 10 CFU/mL) achieved 100% detection for inocula > 1 CFU/mL. Finally, we discuss the applicability of the Dean-migration mechanism and the potential integration of our microfluidic separation device into existing closed GMP-in-a-box cell-therapy workflows.

Materials and methods

Theoretical background

Particles in a spiral flow channel are subjected to two main forces in the direction perpendicular to the main flow, (i) inertial lift (F_L) and (ii) Dean force (F_D)^{12,27,28}. Among them, inertial lift is the combined force of wall-induced inertial lift (F_{LW}) and shear-induced inertial lift (F_{LS}). The shear-induced inertial lift (F_{LS}) pointing toward the wall, induced by the parabolic-shaped velocity profile of the Poisson lobe flow, and the wall-induced inertial lift (F_{LW}) driving the particle away from the wall (pointing toward the center of the flow channel) due to the symmetric trails of the particle rotations near the wall,



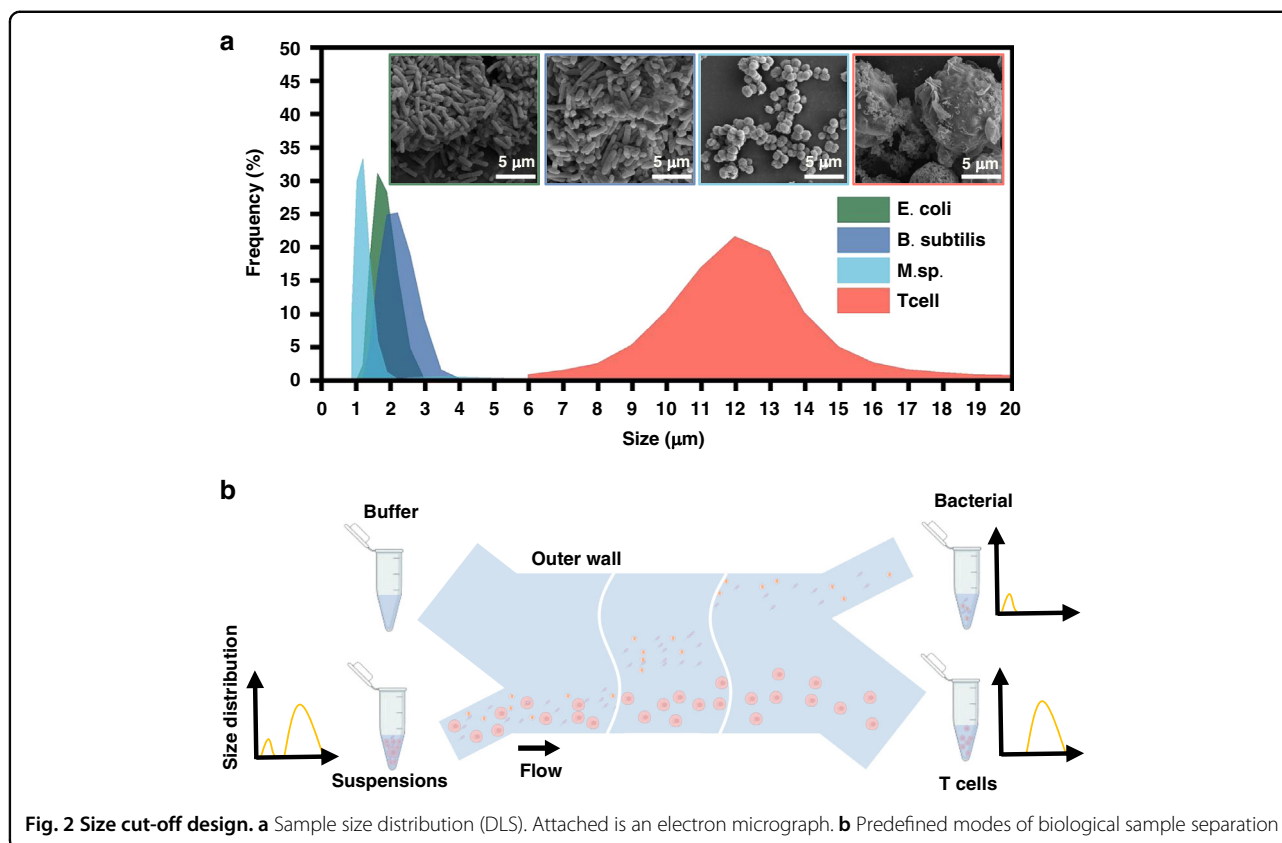
induced by the wall influence, show a position dependent property, with the particles close to the centerline of the flow channel near the shear-induced inertial lift (F_{LW}) and shear-induced inertial lift (F_{LS}). Lift (F_{LS}) is dominant and wall-induced inertial lift (F_{LW}) is dominant near the wall surface of the particle. The inertial lift equation is given by^{29,30}:

$$FL = \frac{\rho U_m^2 a_p^4}{L_c^2} f_L(Re, X_p)$$

where a_p is the characteristic length (diameter) of the particle, L_c is the characteristic length of the channel, and U_m is the maximum flow velocity of the fluid (which can

be estimated by doubling the average characteristic flow velocity U_f). f_L is the dimensionless lift coefficient, which shows position dependence and is generally estimated by taking the mean value of 0.5. Re is the channel Reynolds number for comparing inertial and viscous forces, which is calculated by the formula $Re = \frac{\rho U_m L_c}{\mu}$, where ρ is the fluid density, v is the flow velocity, and μ is the viscosity coefficient.

In the curved microfluidic channel, the particles are not only subjected to inertial forces but also to Dean forces. Dean force, caused by the curvature of the channel, generates counter-rotating vortices known as Dean vortices^{14,27}. These vortices induce a secondary flow perpendicular to the primary axial flow, leading to lateral



particle migration. The strength of the Dean force is measured by the dimensionless constant Dean number (De)³¹, which is defined as $De = Re\sqrt{(L_c/2R)}$, where R is the radius of curvature. The scale expression for the Dean force is as follows²⁸:

$$F_D \propto \frac{\rho U_m^2 a_p L_c^2}{R}$$

Alternatively, the magnitude of this transverse force can be simply estimated by assuming a Stokes trailing force given by the equation¹⁸ $FD = 3\pi\mu a_p U_D$, where $U_D = 1.8 \times 10^{-4} De^{1.63}$ refers to the Dean migration velocity¹⁷. The inertia force equation can be expressed as $F_L = \frac{2Re^2\mu^2}{\rho} \left(\frac{a_p}{L_c}\right)^4$ and the Dean force scale expression can be expressed as $F_D \propto \frac{4Re^2 a_p \mu^2}{\rho R}$. It is not difficult to see that the flow conditions (Re) and the characteristic lengths (a_p , L_c) are the key factors affecting the magnitude of the inertia and Dean forces. It has been widely accepted to replace the characteristic length L_c with the height h in low depth-to-width ratio flow channels^{13,17,31}.

Size cut-off design

To optimize the design of the separation chip, it is essential to first analyze the particle composition of the sample, particularly the particle size distribution of each

component (Fig. 2a). Additionally, a detailed investigation of the forces acting on particles of different sizes within the microfluidic channel is required to clarify their behavior in the flow field and enhance separation efficiency. The particle size range of cultured T cells was measured using a cell counter (Countess, Thermo Fisher Scientific), while the particle size distributions of *Micrococcus* sp., *Escherichia coli*, and *Bacillus subtilis* were determined using dynamic light scattering (Zeta sizer Pro, Malvern Panalytical). The sizes of *Micrococcus* sp., *Escherichia coli*, and *Bacillus subtilis* were measured during their logarithmic growth phase. This growth stage was selected because bacterial cells during this period maintain relatively uniform morphology, stable size distributions, and high metabolic activity, which are representative of potential bacterial contaminants encountered in actual bioprocesses. The results showed that the particle sizes of the three bacterial species ranged from 0.5 to 3 μm , leading to the designation of 0-3 μm as the target size range for removal. Meanwhile, the size range of T cells was determined to be 7-20 μm , with 7 μm set as the threshold for particles to be retained. According to the principle of inertial focusing ($a_p/h \geq 0.07$), 7 μm particles are dominated by inertial forces, rapidly focusing at equilibrium positions upon entering the channel and eventually being collected at the inner-wall outlet (Outlet

1). In contrast, 0–3 μm particles are primarily influenced by Dean forces. These particles are initially confined near the inner wall by the sheath flow upon entering the channel and subsequently undergo lateral migration due to Dean drag, ultimately being collected at the outer-wall outlet (Outlet 2) (Fig. 2b). After establishing the separation model and introducing the sample, T cells remained consistently focused along the inner side of the channel, while bacteria gradually migrated toward the outer wall.

Microdevice fabrication

The device was fabricated using standard soft lithography, comprising a layered structure formed by bonding polydimethylsiloxane (PDMS, Sylgard184, Dow Corning) to a glass substrate. The device features dual-inlet/dual-outlet spiral microchannels with curvature radii ranging from 9.0 to 12.0 mm. The rectangular cross-section channels measure 400 μm in width and 90 μm in height, with a total length of 14.4 cm. The inlet of the sample and the outlet of bacteria (Outlet2) were designed with 80 μm width. The PDMS prepolymer (1: 10 ratio) was poured onto a 4-inch glass wafer and thermally cured at 85 $^{\circ}\text{C}$ for 90 minutes. The cured PDMS replica was peeled off and perforated using 1.6 mm biopsy punches for the inlets/outlets. Surface activation was achieved through a 30 s oxygen plasma treatment (PDMS and glass substrate), followed by pressurized bonding and 60 min annealing at 65 $^{\circ}\text{C}$ on a hot plate to improve interfacial adhesion.

Device characterization

Fluorescent polystyrene microspheres with specified sizes (1, 2, 3, and 7 μm ; 10^5 – 10^6 particles/mL) (Beisile, Tianjin, China) were introduced into the sample inlet using a syringe pump (Harvard Apparatus PHD Ultra, USA) at different flow rates (50–100 $\mu\text{L}/\text{min}$). The sheath buffer, composed of phosphate-buffered saline (GIBCO, USA) supplemented with 0.1% bovine serum albumin (bio-smlile, China), was delivered into the sheath inlet via a separate syringe pump. The setup was mounted on an inverted fluorescence microscope (IX71, Olympus) and used to visualize the equilibrium positions of beads of different sizes through fluorescence imaging. Before and after each experiment, the chip was cleaned with 1% (w/v) Pluronic F127 for 10 minutes. After cleaning, both the sample and sheath inlets were pre-flushed with sheath buffer at the preset flow rate for 10 minutes, after which the sheath buffer at the sample inlet was replaced with the sample solution.

Cell culture

The Jurkat cell line (human T-lymphocytes, ATCC TIB-152) was maintained in RPMI 1640 medium (GIBCO, USA) supplemented with 10% fetal bovine serum (Gibco, USA) and 1% penicillin-streptomycin solution (Gibco,

USA), cultured at 37 $^{\circ}\text{C}$ under 5% CO_2 in a humidified incubator (Thermo Heracell 150i, USA). Subculturing was performed every 72 h at 1:3 split ratio, maintaining cell density between 0.5 – 1×10^6 cells/mL (Cell density before expansion). Experimental bacterial strains (*Escherichia coli* BNCC361247, *Bacillus subtilis* BNCC109047, *Micrococcus sp.* BNCC360943) were inoculated in LB broth (BD Difco, USA) and cultured in a shaking incubator (New Brunswick Innova 42, USA) at 37 $^{\circ}\text{C}$ with 200 rpm agitation. Optical density measurements (OD_{600}) were recorded every 2 hours using a microplate reader (Tecan, GENios Plus, Switzerland) to monitor growth curves, with bacterial logarithmic phase cultures selected for subsequent experiments.

Sample preparation

To simulate authentic contamination scenarios in T-cell culture systems, this study employed bacterial particles as contaminants. T-cells were quantified using a cell counter (Countess, Thermo Fisher) prior to experimentation. To approximate the real situation, samples were directly collected from culture flasks without concentration or resuspension. Cell concentrations ranged from 2×10^6 to 10×10^6 cells per mL, typically around 6×10^6 cells per mL. Bacterial strains (*Micrococcus sp.*, *Escherichia coli*, *Bacillus subtilis*) were cultured to log-phase growth, followed by optical density (OD) measurement and SYTO BC Green (Thermo Fisher Scientific, USA) fluorescent dye staining. After 10 min incubation at 37 $^{\circ}\text{C}$ under dark conditions, bacteria were washed thrice with PBS and diluted to 10^7 CFU/mL. Subsequently, 10 μL bacterial suspension was spiked into 1 mL T-cell suspension to prepare mixed contamination samples with final bacterial concentration of 10^5 /mL. Before each separation experiment, individual T-cell samples, single bacterial suspensions, and contamination samples were freshly prepared. Contaminated samples are single bacteria mixed with T cells. Microfluidic separation was performed using 1 mL mixed samples, with post-separation fractions collected from both outlets. Flow cytometric analysis was conducted using 5 μL CD45-PE antibody (Thermo Fisher Scientific, USA) for T-cell labeling, involving 30 min room temperature incubation under dark conditions prior to detection. All procedures were executed under aseptic conditions to ensure data reliability and experimental reproducibility.

Isolation of bacterial from T cell cultures

Prior to experiments, microchannels were perfused with 1% (w/v) Pluronic F127 solution at 1.5 mL/min for 10 min. During system equilibration, sheath fluid (PBS containing 0.1% (w/v) BSA) was infused at predetermined flow rates (sample inlet: 50–100 $\mu\text{L}/\text{min}$; sheath inlet: 600–700 $\mu\text{L}/\text{min}$) for 10 min until pressure fluctuations

stabilized. The sample suspension was then introduced using a Harvard Apparatus Pump 11 Elite with continuous infusion for 20 min. The experimental setup incorporated a fluorescence microscope (IX71, Olympus) coupled with a high-speed imaging system (XGV-Cam, Hefei Thousand-eye Wolf, China) capturing phase-contrast micrographs at 10,000 fps (resolution 1280×1024) to analyze spatial distribution of cells and bacteria at outlets (Supplementary Videos 2–3).

Flow cytometry

Flow cytometry analysis was performed using an Attune NxT acoustic focusing flow cytometer (Thermo Fisher Scientific, USA) to achieve absolute quantification of particle concentrations via a fixed-volume sampling method (50–200 μL), thereby circumventing the need for standard bead calibration. The detection process comprised: (i) Independent analysis of single samples (T cells, *Escherichia coli*, *Micrococcus* sp., and *Bacillus subtilis*), with particle populations gated based on forward scatter (FSC, 488 nm) and side scatter (SSC, 405 nm) parameters. (ii) Analysis of mixed samples, wherein dual-channel validation of population specificity was achieved using SYTO BC Green fluorescence (a bacterial nucleic acid stain) and CD45-PE red fluorescence (a T cell marker). Separated samples were re-analyzed using the same gating strategy to ensure data comparability. Viable cells ($\text{FSC} > 5 \times 10^2$), dead cells ($1 \times 10^2 < \text{FSC} < 5 \times 10^2$), and individual bacteria ($\text{FSC} < 1 \times 10^2$) exhibited a three-tier gradient distribution in the scatter plots ($\Delta\text{SSC} > 30\%$). A key source of interference arose from overlapping signals in the bacterial gate (FSC/SSC ratio 0.5–0.7) due to cell debris (FSC/SSC ratio 0.8–1.2) and culture medium particles (FSC/SSC ratio 1.5–2.0), which produced approximately $12\% \pm 3\%$ overlap. Specific staining with SYTO BC Green (excitation/emission: 485/530 nm) reduced interference from nonbiological particles to below the detection limit ($< 0.1\%$ positive rate), thereby enabling label-free and precise discrimination in the mixed system of T cells–bacteria.

Fluorescent microscopy detection

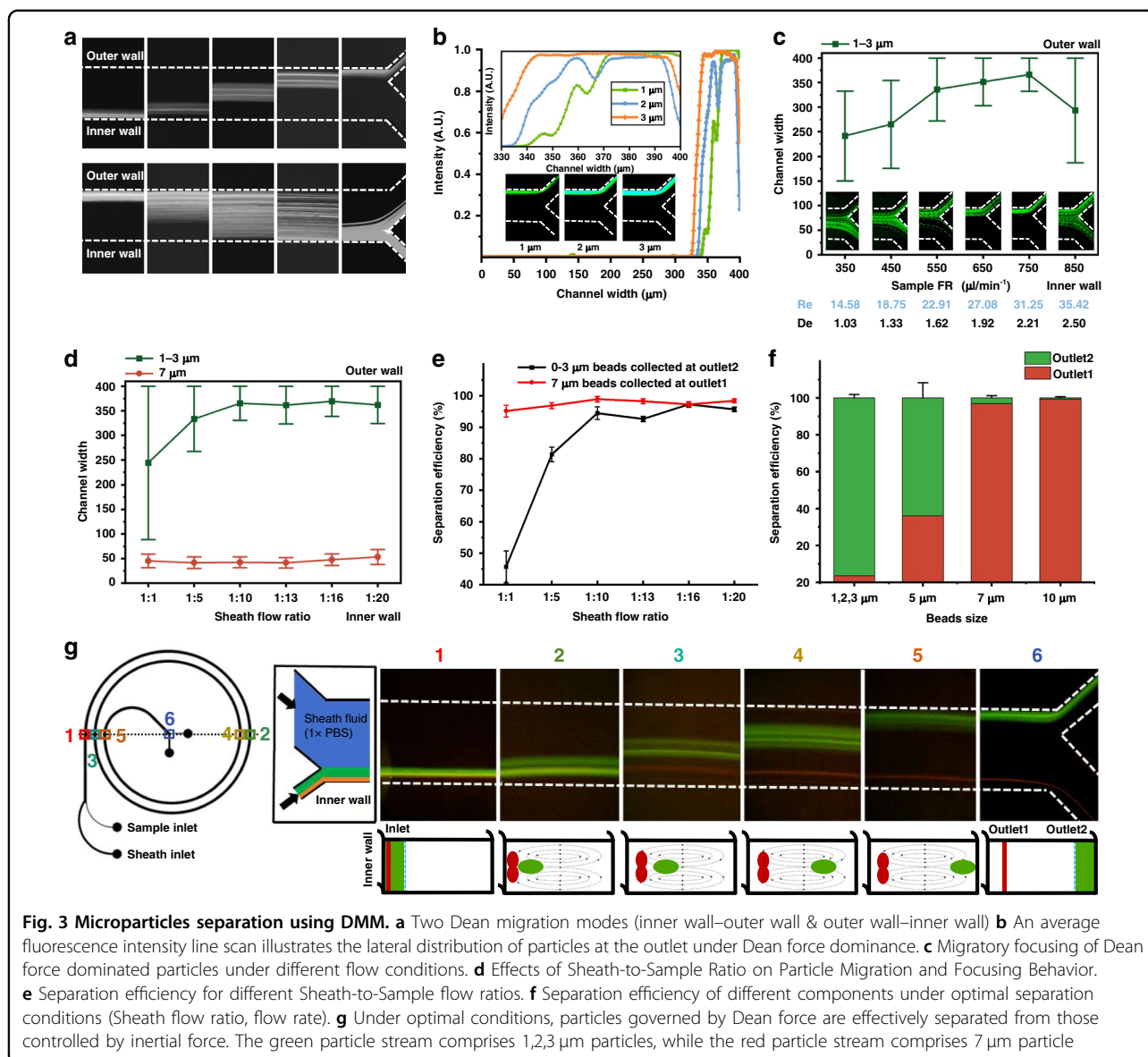
To further validate the efficacy of separation between T cells and contaminants (bacteria), post-separation samples were prepared on microscope slides. Automated fluorescence microscopy (BZ-X800LE, Keyence) equipped with $20\times/0.95$ NA and $40\times/0.95$ NA objectives was employed for imaging. Morphological characteristics were recorded in the bright field mode, while fluorescent signals were acquired through the FITC channel (excitation 480/30 nm, emission 535/40 nm). Image processing, particle enumeration, and fluorescence quantification were performed using ImageJ to evaluate separation efficiency and bioparticle distribution patterns.

Results and discussion

MPs separation using DMM

Based on the inertial focusing principle ($a_p/h > 0.07$), spiral microfluidic devices can focus or separate particles exceeding specific size thresholds. Sheath flow confinement of the initial particle position enables acquisition of larger-component samples with cleaner backgrounds. However, unfocused particles ($a_p/h < 0.07$) and atypical-sized particles ($a_p \leq 5 \mu\text{m}$) remain understudied. To study particles defying the inertial focusing principle, the sample inlet was positioned at the channel inner wall with sheath flow inlets at the outer wall, making lateral migration of non-focusing particles the sole observable transverse motion. This configuration confines particle initial positions to the inner wall, enabling inertia-focused particles to stabilize at equilibrium positions near the wall under inertial lift force (F_L), while Dean force (F_D)-dominated particles undergo outward-directed lateral migration. We thus define this Dean force driven lateral migration strategy for small particle sorting as the Dean Migration Mechanism (DMM).

Dean vortices form two counter-rotating symmetric vortices in the direction perpendicular to the main flow. Small particles dominated by Dean force migrate from the inner wall to the outer wall along the symmetry line (the centerline of the channel cross-section) of these vortices. In contrast, the migration from the outer wall to the inner wall is more complex, as originally focused particles are dragged by the vortices from the top and bottom symmetric positions of the channel cross-section toward the inner wall (Supplementary Fig. S1). To validate these two migration modes induced by Dean drag, we designed and tested another microfluidic chip with the same spiral geometry but with the sample inlet located at the outer wall, thereby characterizing the two Dean migration processes (Fig. 3a). To gain a deeper understanding of the motion patterns of contaminant particles within the microfluidic channel, we introduced 1, 2, and 3 μm fluorescent beads and found that these particles all underwent Dean-driven lateral migration from the inner wall to the outer wall. At the outlet, these particles adhered closely to the outer wall, and the width of the particle stream increased slightly with particle size, although the width difference was less than 10 μm (Fig. 3b). Next, we investigated the migration and focusing behavior of particles under different flow rate conditions (Fig. 3c). With a fixed sample flow rate of 50 $\mu\text{L}/\text{min}$, the sheath flow rate was varied between 350 and 750 $\mu\text{L}/\text{min}$. As the flow rate increased, the green fluorescent particle stream gradually shifted from the center of the channel toward the outer wall, and the stream width progressively decreased. When the flow rate reached 750 $\mu\text{L}/\text{min}$, the 1, 2, and 3 μm particles ultimately formed a narrow band with a width of approximately 80 μm (close to the sample



inlet width). However, further increasing the flow rate resulted in defocusing and the reoccurrence of lateral migration toward the inner wall, indicating that the narrow band structure driven by Dean force is not a stable equilibrium state but rather adjusts with the periodic variation of the Dean force. Under the optimized flow conditions (750 $\mu\text{L}/\text{min}$), we further explored the relationship among particle focusing width, sheath flow ratio, and initial particle position (Fig. 3d). With the total flow rate fixed at 750 $\mu\text{L}/\text{min}$, as the sheath flow ratio increased, the outlet position of the 1–3 μm (green) particle stream gradually narrowed and stabilized when the sheath-to-sample ratio reached 1:10, with the particle stream width at both the inlet and outlet remaining around 80 μm . In contrast, 7 μm particles (red)

maintained a stable inner-wall focusing under inertial force, with a width of approximately 25 μm . Finally, we characterized the separated fluorescent beads using flow cytometry. The results showed that the separation efficiency of 1, 2, and 3 μm particles increased with the sheath flow ratio and stabilized at around 95% once the ratio reached 1:10, while the separation rate for 7 μm particles remained above 95% (Fig. 3e).

Under optimal separation conditions, migration patterns of both particle types were imaged at 0.5 spiral loop intervals (Fig. 3g and Supplementary Video 1). Dean force-governed particles (1, 2, 3 μm) migrated along narrow bands from inner to outer channel walls, ultimately collected through Outlet 2. All three particle types exhibited similar narrow-band migration patterns,

indicating Dean-driven lateral velocity independence from particle size (as reported by Hui Min Tay et al.²²). This aligns with the empirical Dean velocity formula $U_D = 1.8 \times 10^{-4} De^{1.63}$ derived from numerical simulations by Ookawara et al.^{32,33}. Conversely, 7 μm particles maintained stable inner-wall focusing under inertial dominance, collected via Outlet 1. Both particle types formed distinct focusing bands at channel sides with clear separation streamlines at outlets, separated by wide buffer zones. Separation capability was validated using 1–3 μm particles (10^5 /mL) mixed with 5/7/10 μm particles (10^6 /mL), quantified via flow cytometry (Fig. 3f). Results showed >95% separation efficiency for both Dean-dominated (1–3 μm) and inertial-dominated (7,10 μm) particles. Near-critical $a_p/h = 0.07$ (5 μm particles) showed compromised separation, with outlet statistics significantly differing from both inertial- and Dean-dominated populations ($P < 0.01$). This suggests 5 μm particles exist in transitional state with combined Dean-inertial force competition/coupling, lacking full dominance for periodic migration or equilibrium focusing. We therefore classify particles into three regimes: Dean-dominated, inertial-dominated, and Dean-inertial competitive particles.

Effect of characteristic length on particle migration and focusing

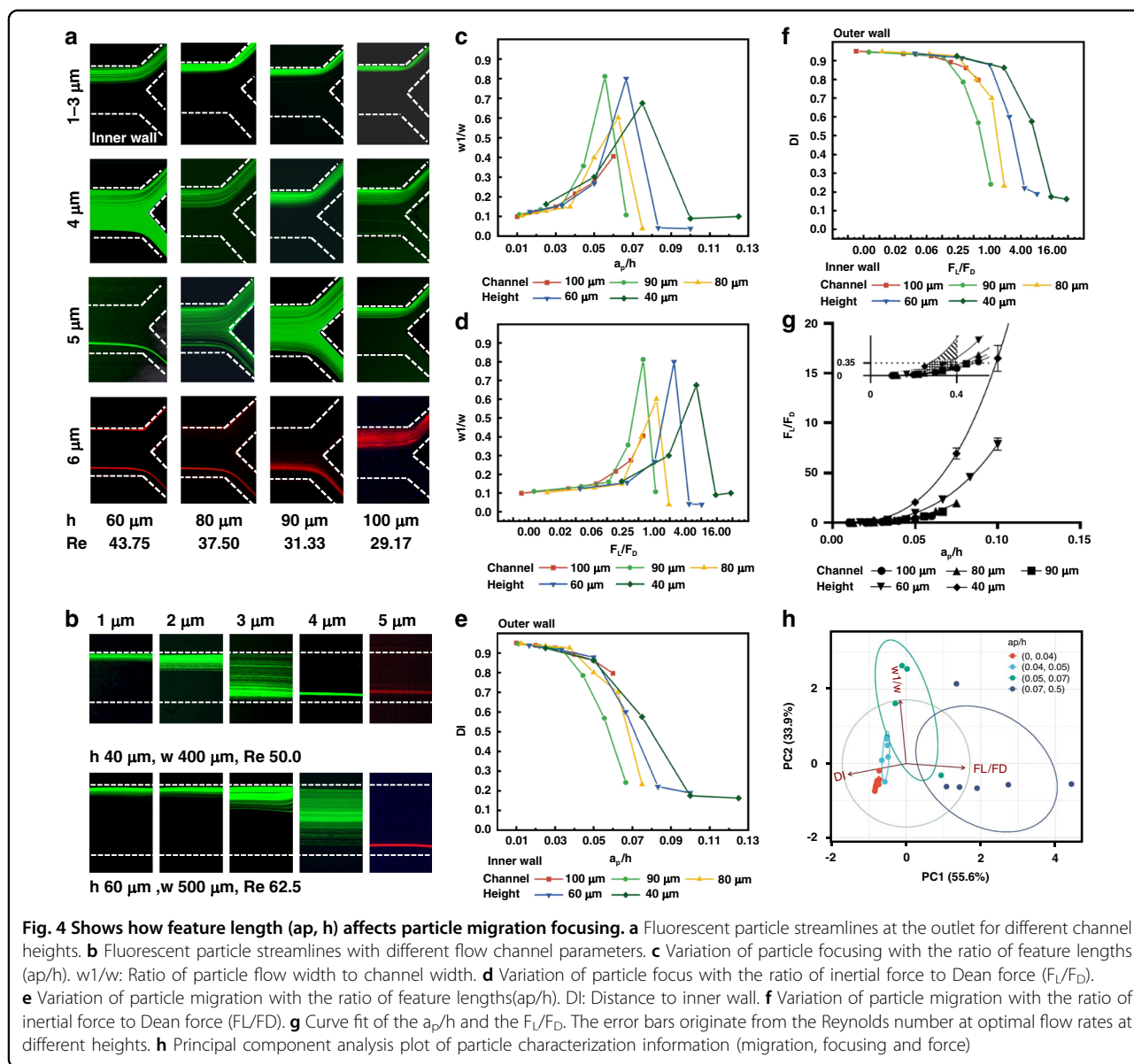
To investigate the effect of aspect ratio a_p/h on atypical particle ($a_p/h < 0.07$) migration/focusing, microchannels with identical geometry but varying heights (60, 80, 90, 100 μm) were fabricated and tested with fluorescent particles of different sizes. The optimal flow rate was defined as the velocity enabling 1 μm particles to exit through the outer-wall outlet as a narrow band adhering to the channel wall. Particles exhibiting lateral migration under Dean drag force and forming wall-adherent narrow bands at the channel exterior were identified as Dean-force dominated. Experiments at optimal flow rates across channel heights employed color-camera fluorescence imaging at outlets (Fig. 4a). Fluorescent images revealed Dean-dominated particles consistently focused on outer walls across all channel heights, forming tightly-adherent narrow streams. Inertial-dominated particles focused at inner-wall equilibrium positions forming ultra-narrow streams. Particles under combined force competition formed wider, unfocused streams. Non-focused streams across heights exhibited a_p/h ratios 0.05–0.07 (Supplementary Fig. S3), while Dean-dominated particles maintained $a_p/h < 0.05$.

Verification experiments fabricated 40 μm height channels and geometrically modified 60 μm channels. The 40 μm channel enabled Dean-dominated focusing of 1–2 μm particles at outer walls (2 μm : $a_p/h = 0.05$), while 3 μm particles showed loose inner-wall focusing and

larger particles exhibited tight equilibrium focusing (Fig. 4b). These findings preliminarily confirm both principles hold for lower-height and geometrically-modified channels: combined-force particles require $0.05 \leq a_p/h \leq 0.07$, while Dean-dominated particles need $a_p/h < 0.05$.

To further validate the effect of aspect ratio a_p/h on atypical particle migration/focusing, the normalized distance (DI) from stream center to inner wall quantified migration behavior, while normalized stream width ($PW = \text{particle stream width/channel width}$) evaluated focusing performance. The aspect ratio a_p/h primarily determines inertial lift force $F_L = \frac{2Re^2\mu^2}{\rho} (\frac{a_p}{h})^4$. Previously, in the field of inertial focusing, some researchers proposed that the ratio $R_f = F_L/F_D$ could be used to quantify particle focusing. $R_f = \frac{F_L}{F_D} \propto \frac{1}{\delta} (\frac{a_p}{h})^3 f_L(Re, X_p)$, where $\frac{1}{\delta}$ means $\sqrt{(L.c/2R)}$. We refined particle classification by incorporating Dean force variations, necessitating combined analysis of inertial and Dean forces. Particle stream width across channel heights initially increased then decreased with aspect ratio a_p/h , forming bell-shaped curves. Low a_p/h (< 0.04) corresponded to Dean-dominated focused streams with high consistency, while high a_p/h produced narrower inertial-dominated streams. Peak values represented unfocused streams under force competition, clustered at a_p/h 0.05–0.07 (Fig. 4c). R_f dependent stream width variations mirrored aspect ratio-dependent patterns across channel heights. Unfocused particles exhibited $R_f \approx 1$ at peak positions, theoretically confirming Dean-inertial force competition. Notably, inertial-dominated particles consistently showed $R_f \geq 1$. Both R_f and a_p/h dependent curves showed rightward peak shifts with decreasing channel height (Fig. 4d).

The lateral position of particles at the channel outlet progressively shifts toward the inner wall as the characteristic size-to-height ratio (a_p/h) increases (Fig. 4e). When a_p/h ranges from 0 to 0.04, particles consistently migrate and focus near the outer channel wall, indicating dominant Dean-driven lateral displacement. As a_p/h increases from 0.04 to 0.05, particles begin to exhibit a noticeable shift toward the inner wall. When a_p/h falls within the range of 0.05 to 0.07, particle streams are located near the channel centerline, and when a_p/h exceeds 0.07, particles predominantly focus near the inner wall. This migration behavior is modulated by the force ratio R_f . As R_f increases, inertial lift gradually overcomes Dean drag, causing particles with intermediate a_p/h values (0.04–0.05) to deflect from tight Dean-focusing and form loosely clustered bands near the outer wall. With further increase in R_f , particles within a_p/h of 0.05–0.07 fall into a force-competition regime, where neither Dean drag nor inertial lift dominates, resulting in unfocused, dispersed streams. Eventually, when inertial forces dominate, particles settle into well-defined equilibrium positions near the inner wall. Notably, all particles focused near the inner



wall under inertial-dominant conditions satisfy $R_f \geq 1$ (Fig. 4f), whereas particles focused near the outer wall under Dean-dominant conditions consistently exhibit $R_f \leq 0.25$. Furthermore, curves describing lateral position versus a_p/h shift rightward as channel height decreases. Although identical a_p/h values yield different R_f values across channel heights, high consistency is preserved when R_f is low. Specifically, Dean-dominated particles simultaneously satisfy $a_p/h < 0.04$ and $R_f < 0.35$ across all tested configurations (Fig. 4g).

Principal component analysis (PCA) was performed on particle characteristics (lateral position, focusing degree, inertial/Dean force ratio, a_p/h) across channel heights (Fig. 4h). Color-coded clusters representing experimental groups showed decreasing similarity with increasing

Euclidean distance in PCA space, demonstrating significant inter-group differences. Within 40–100 μm channels, particles with $a_p/h \leq 0.05$ exhibited Dean-force dominance, particularly those with $a_p/h \leq 0.04$ forming tightly-packed wall-adherent streams at outer walls. Particles with $0.04 < a_p/h \leq 0.05$ showed semi-focused streams due to emerging inertial effects. The 0.05–0.07 a_p/h range produced unfocused broad streams under Dean-inertial force competition. The 90 μm channel optimized target particle (contaminants) sorting: 1–3.6 μm particles formed tight outer-wall streams under complete Dean dominance, while 3.6–4.5 μm particles displayed looser streams with emerging inertial effects. Outlet ratio adjustment to 1: 4 enabled Outlet2 to collect particles within 80 μm from outer wall.

Effect of flow condition on particle migration and focusing

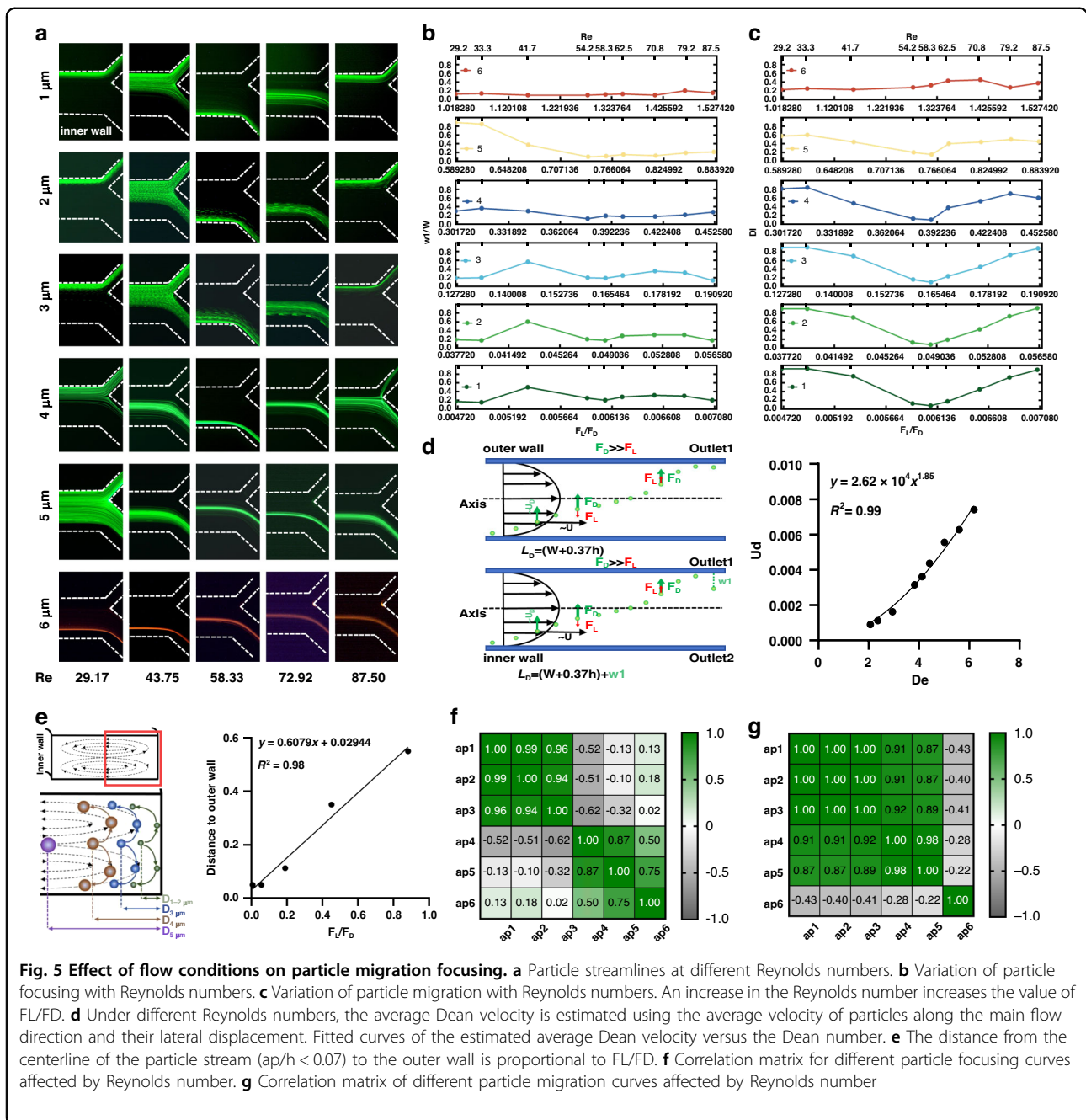
Inertial focusing typically occurs at Reynolds numbers $Re = 30$ – 100 . Subthreshold Re (<30) causes insufficient inertial lift forces, leading to unfocused particles despite meeting geometric focusing criteria. Dean force-dominated particles undergo cyclic lateral displacements under Dean drag. Finite channel limitations were overcome by flow condition optimization to observe this periodic motion. In $90\ \mu\text{m}$ -height channels with fixed sample flow ($50\ \mu\text{L}/\text{min}$) and sheath flow (650 – $2050\ \mu\text{L}/\text{min}$), outlet fluorescence imaging was performed using a color camera (Fig. 5a). Focusing degree was quantified by W_1/W ratio (Fig. 5b), while lateral position was evaluated using normalized DI (Distance to inner wall) (Fig. 5c). The force ratio $R_f = F_L/F_D$ increased with Re , indicating enhanced inertial effects at higher Reynolds numbers. Particles with $a_p/h < 0.04$ (1 – $3\ \mu\text{m}$) under complete Dean dominance were confirmed to undergo cyclic lateral displacements. Focusing degree exhibited initial enhancement followed by decay during migration, regardless of starting position (Fig. 5b). Notably, minimal lateral position variation with enhanced focusing was observed at $Re = 29.17$ – 33.33 . This stems from Dean-dominated particles requiring additional Z-direction displacement (Fig. S1) after crossing Dean vortex symmetry lines ($0.5h$) during wall-to-wall migration. The phenomenon persisted during inward migration ($Re = 58.33$). Experimental lateral position data enabled derivation of mean Dean velocity: $U_D = 2.62 \times 10^{-4} De^{1.85}$, $R^2 = 0.99$ (Fig. 5d).

For particles with a_p/h between 0.04 and 0.05 ($4\ \mu\text{m}$), which are primarily influenced by Dean force but begin to experience the effects of inertial force, their lateral migration curves at the outlet, as Reynolds number increases, resemble those of fully Dean force-dominated particles (1 – $3\ \mu\text{m}$). However, when migrating to a position near the channel wall ($Re = 58.33$, 87.5), these particles fail to adhere closely to the wall, and their distance from the wall increases with rising Reynolds number. This phenomenon is attributed to the wall-induced inertial lift force (F_{LW}), which pushes them away from the channel wall. Interestingly, for particles under the competition of both forces ($5\ \mu\text{m}$), the initially unfocused particle stream transitions into a focused stream as the Reynolds number increases (Fig. 5b). Moreover, when Re exceeds 58.33 , their migration behavior becomes more similar to that of inertial force-dominated particles ($6\ \mu\text{m}$) (Fig. 5c). This transition occurs because, as the Reynolds number increases, the ratio of inertial force to Dean force (F_L/F_D) also rises, leading to inertial force gradually becoming the dominant factor. As a result, these particles in the regime of competing forces gradually become dominated by inertial force as the Reynolds number increases. At a Reynolds number of 87.5 , Dean force-dominated particles migrate back to the outer wall, forming a narrow band

closely adhering to the channel wall. At this stage, all tested particles (1 – $6\ \mu\text{m}$) maintain a high degree of focusing, and their lateral positions exhibit a linear correlation with F_L/F_D ($R^2 = 0.98$) (Fig. 5e). At the same time, this may also be a potentially high-resolution manipulation, although the effect of the higher sheath-fluid ratio (30 – 40) is an issue that needs to be overcome.

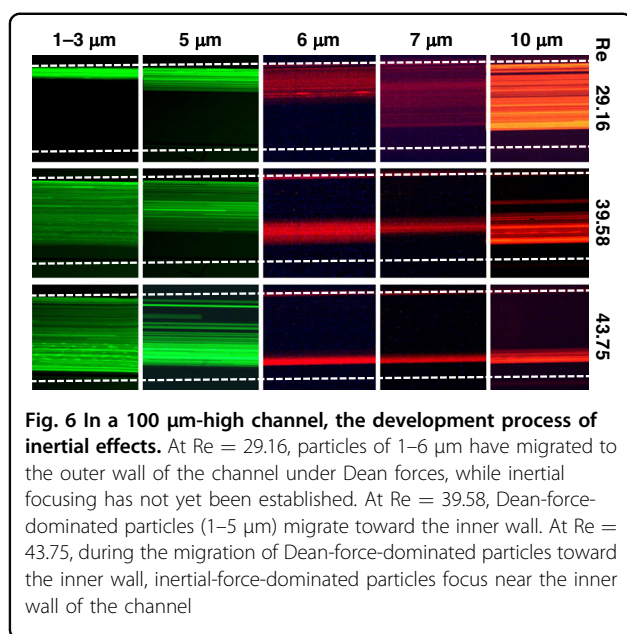
For inertial force-dominated particles ($\geq 6\ \mu\text{m}$), the particle stream remains highly focused at all tested Reynolds numbers (Fig. 5b). Their lateral equilibrium positions shift toward the channel centerline as the Reynolds number increases. This phenomenon arises because, at the equilibrium position, the particles experience a balance among three forces ($F_{LS} = F_{LW} + F_D$). In this force balance, the position-dependent nature of the inertial force and the increasing influence of Dean force lead to a shift in the equilibrium position (Supplementary Fig. S2). The experiments conducted in a $90\ \mu\text{m}$ -high channel reveal that particles with different characteristic length (a_p/h) exhibit distinct migration and focusing behaviors. To further validate this classification, researchers constructed a correlation matrix based on the migration and focusing data of 1 – $6\ \mu\text{m}$ particles. A higher correlation value indicates a stronger relationship between the migration behaviors of two particle groups, suggesting a higher likelihood that they belong to the same mechanical classification (Fig. 5f–g). The researchers also demonstrated changes in the correlation based on Reynolds number segments (Supplementary Fig. S2), which confirms that the inertial force effects intensify with increasing Reynolds number. The results clearly show a strong correlation in migration and focusing curves among 1 – $3\ \mu\text{m}$ particles. As particle size increases (and thus the characteristic length ratio increases), the ratio of inertial force to Dean force (F_L/F_D) increases significantly, demonstrating a continuous transition from Dean force-dominated behavior (1 – $3\ \mu\text{m}$) to inertial force-dominated behavior ($>6\ \mu\text{m}$). In this transition, $4\ \mu\text{m}$ and $5\ \mu\text{m}$ particles represent two typical intermediate states: $4\ \mu\text{m}$ particles remain primarily influenced by Dean force but begin to experience inertial effects, while $5\ \mu\text{m}$ particles are in a competitive regime where both forces exert significant influence.

However, experiments with particles in a channel $100\ \mu\text{m}$ high showed that not only particles in the 1 – $4\ \mu\text{m}$ range, but even particles 5 , $6\ \mu\text{m}$, exhibited Dean force dominated migration, accumulating at the outer wall of the channel. This deviates from the repeatedly validated pattern observed at other channel heights, where Dean force-dominated migration typically occurs in particle populations with $a_p/h < 0.04$ (Fig. 4a). Furthermore, experiments using particles 7 , $10\ \mu\text{m}$ (which satisfy the inertial focusing condition) revealed that, at the current Reynolds number ($Re = 29.33$),



these particles failed to focus on the inner wall and instead displayed a diffuse distribution throughout the channel (Fig. 6). As the Reynolds number increased, the strengthening inertial force gradually restored inertial focusing. This indicates that, under low Reynolds number conditions, the inertial lift is insufficient to maintain stable focusing (Fig. 6). Experiments conducted in channels with other heights similarly demonstrated that, under low Reynolds number conditions, the Dean force-dominated migration mode (DMM) remains effective (Fig. 3d). Specifically, low

Reynolds numbers result in even particles that satisfy $a_p/h > 0.07$ being unable to undergo inertial focusing, while particles that are in the competitive regime between inertial and Dean forces ($0.04 < a_p/h < 0.07$)—due to inadequate inertial force—become dominated by Dean force and exhibit lateral migration. These findings indicate that intentionally reducing the Reynolds number can minimize inertial effects, thereby enabling controlled lateral migration of particles $a_p/h < 0.06$ (approximately the threshold) under the influence of Dean force.



Size fractionation of T-cell cultures with bacterial contamination

To address the complexity of potential contaminants in cell culture processes—including bacteria (0.5–5 μm), viruses (20–300 nm), and protein aggregates—we selected bacteria as a representative model for separation studies. Given the morphological diversity of bacteria and the size-based nature of our passive sorting approach, we selected three bacterial species with distinct shapes and sizes: cocci (*Micrococcus* sp.), short rods (*Escherichia coli*), and long rods (*Bacillus subtilis*), to evaluate the device's separation performance.

In clinical cell therapy production, typical sample volumes for sterility and quality testing range from 1–3 mL, or approximately one-tenth of the culture volume. Therefore, the sampling volume in our experiments was set to 1 mL. Based on our empirical model, a microchannel height of 90 μm was selected to ensure that particles smaller than 3.6 μm remain in the Dean flow-dominant regime, facilitating effective separation.

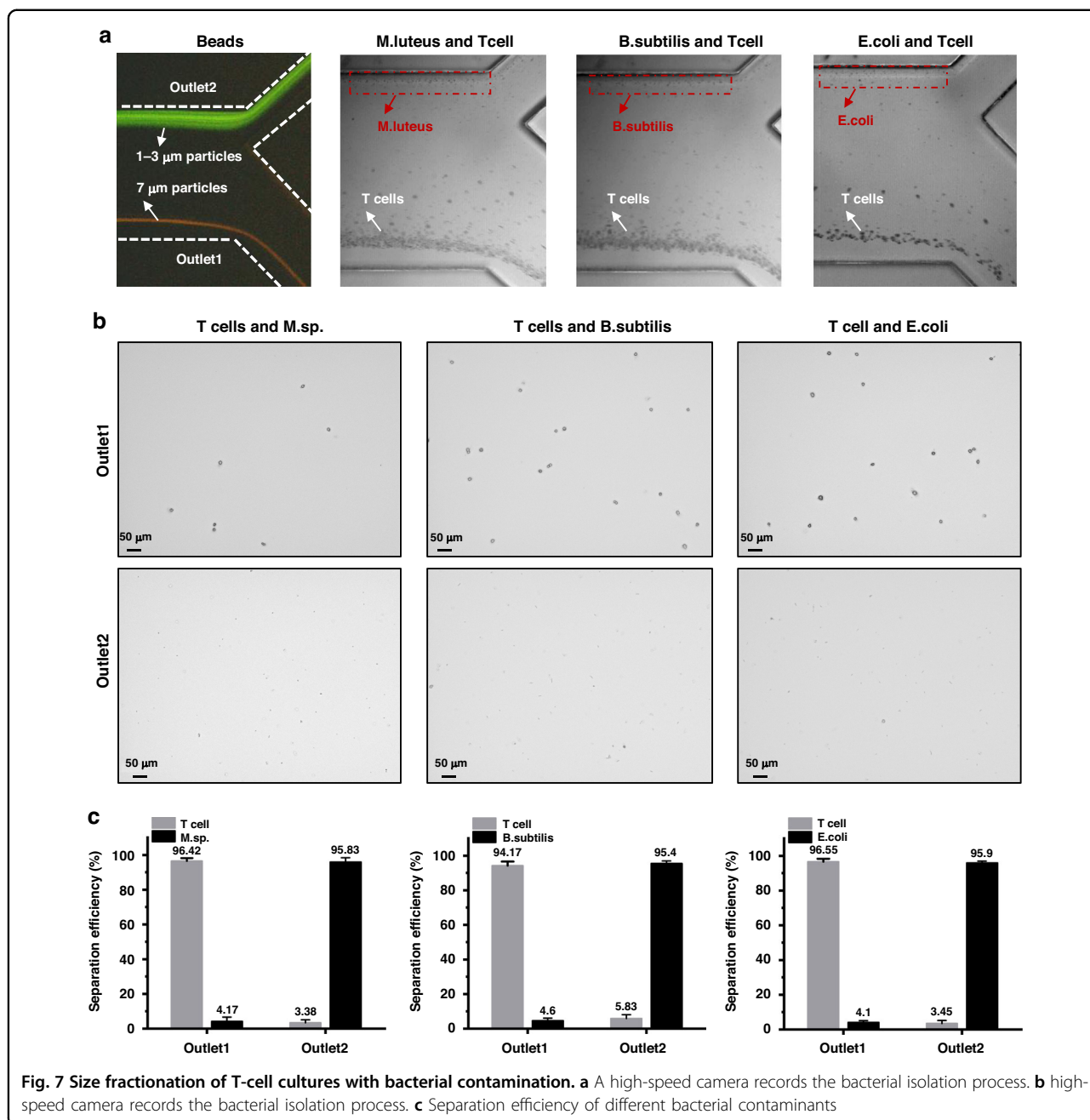
The device's separation performance was first validated using a mixture of fluorescent microparticles (1–3 μm and 7–10 μm), which were efficiently sorted into distinct outlets with high recovery and purity. To verify its applicability to biological samples, a mixed suspension of bacteria (10^5 CFU/mL for each strain) and T cells (10^6 cells/mL) was prepared. The mixture was injected into the sample inlet at 50 $\mu\text{L}/\text{min}$, while phosphate-buffered saline (PBS) containing 2.5% EDTA and 1% BSA served as the sheath fluid, introduced at 750 $\mu\text{L}/\text{min}$. High-speed imaging (10,000 frames/s) was employed to monitor the separation dynamics at the outlets (Fig. 7a).

Under the influence of Dean forces, all bacterial species focused near the outer wall of the spiral channel, consistent with microparticle behavior. Fluorescence microscopy analysis confirmed that bacterial particles (0.5–3 μm) were collected at the outer outlet (Outlet 2), while larger T cells (≥ 6 μm), dominated by inertial forces, were directed toward the inner outlet (Outlet 1), consistent with the theoretical predictions and bead separation results (Fig. 7a). Flow cytometry analysis demonstrated high separation efficiencies for *Micrococcus* (95.83%), *B. subtilis* (95.40%), and *E. coli* (95.90%), with corresponding T cell depletion rates of 96.42%, 94.17%, and 96.55%, respectively (Fig. 7c). Fluorescence microscopy further verified these results, showing well-defined cell morphology at Outlet 1 and small-sized bacterial particles at Outlet 2 (round for *Micrococcus*, rod-shaped for *E. coli* and *B. subtilis*). Fluorescein isothiocyanate (FITC) fluorescence confirmed the biological nature of the sorted particles, and fluorescence intensity analysis showed strong agreement with flow cytometry data (Fig. 7b and Supplementary Fig. S6).

Finally, we evaluated the potential of the microfluidic online separation method to replace manual offline methods (membrane filtration and centrifugation), in terms of both bacterial purity and recovery rate (Fig. S7).

To evaluate the performance of our device under conditions mimicking bacterial contamination in cell therapy samples, which typically exhibit extremely low bacterial loads (<100 CFU/mL), we conducted experiments using ultra-low bacterial concentrations. Samples were prepared via serial dilution to achieve single- and mixed-species bacterial suspensions at concentrations of 10^2 , 10^1 , and 1 CFU/mL. To simulate a realistic biological background, T-cell cultures were sampled directly from culture flasks after 72 hours, with a cell density of approximately 6×10^6 cells/mL. To minimize sample loss during low-input detection, we optimized the operational workflow: the system was pre-flushed at a predetermined flow rate before sample injection; following a 20 min separation run, 1 mL of 1 \times PBS was drawn through the same syringe and processed for an additional 20 min. The outlet tubing was directly connected to a filtration module, where outlet 2 samples were filtered through a 0.45 μm membrane, while outlet 1 samples were sequentially filtered through 8 μm and 0.45 μm membranes to achieve graded retention of cells and bacteria. After filtration, membranes were placed face-up on agar plates for colony cultivation.

Experimental results demonstrated robust device performance across a wide range of bacterial concentrations. At 10^2 CFU/mL, the device maintained a separation efficiency exceeding 90%. Although colony density on the membranes was too high for precise enumeration, hundreds of colonies were observed on the inlet and outlet 2 membranes, with only sporadic colonies detected on



outlet 1 membranes (Supplementary Fig. S9). Overall, a 100% detection rate was achieved for both single- and mixed-species contamination at low bacterial loads (ranging from a few to hundreds of CFUs). (Fig. 8) At 10^1 CFU/mL, all replicate experiments ($n = 3$) consistently detected *Escherichia coli* at outlet 2. For mixed bacterial suspensions (*Micrococcus* spp. and *Bacillus subtilis*), both species were reliably recovered at outlet 2, with only occasional single *E. coli* colonies observed at outlet 1. At the lowest tested concentration (1 CFU/mL), no *E. coli*

colonies were detected at either outlet, likely due to limitations in sample volume and detection sensitivity. In mixed bacterial suspensions (*Micrococcus* spp. and *B. subtilis*), only *Micrococcus* was recovered at outlet 2, with no detection of *B. subtilis*, potentially attributable to sampling variability or processing losses (Supplementary Fig. S10). These findings confirm the device’s robust performance across a broad concentration range, providing strong evidence for its potential in contamination control within cell therapy manufacturing.

Discussion

A comprehensive understanding and analysis of the forces and motion characteristics of particles with different sizes within the channel is crucial for developing size-based separation methods. This not only significantly enhances separation efficiency but also provides a vital theoretical basis for the design of separation devices, particularly in optimizing key parameters such as channel height and Reynolds number. In this study, the particle manipulation method based on Dean migration is categorized into two regimes according to whether inertial focusing occurs: (i) Low Reynolds number condition: The inertial force acting on particles is insufficient to induce inertial migration. By intentionally reducing the Reynolds number to minimize inertial effects, only particles with $a_p/h < 0.06$, which are dominated by Dean force, undergo

Dean migration. (ii) Moderate Reynolds number condition: Both inertial migration and Dean migration occur simultaneously. Particles satisfying the inertial focusing condition are governed by inertial force and are focused at equilibrium positions, while particles with $a_p/h < 0.04$ are completely dominated by Dean force and form a focused particle stream that exhibits recurrent lateral migration within the channel.

Particles with $0.04 < a_p/h < 0.05$, although predominantly influenced by Dean force, begin to experience inertial effects; consequently, despite undergoing Dean migration, their focusing degree differs significantly from that of particles fully governed by Dean force. Moreover, as the Reynolds number increases, the enhanced inertial influence causes these particles to be repelled from the channel wall by wall-induced inertial lift (F_{LW}), resulting in a greater distance from the wall. Particles with $0.05 < a_p/h < 0.07$ experience a competitive coupling between inertial and Dean forces, leading to a dispersed, unfocused particle stream in the channel. These intermediate-state particles gradually become dominated by inertial force as the Reynolds number increases, exhibiting migration and focusing behaviors similar to those of inertial force-dominated particles.

Although the aforementioned particle migration patterns have been validated under various channel parameters, their general applicability still requires further investigation. To this end, we reviewed spiral microfluidic chips developed by other researchers for small particle separation (Table 1). For example, the high-resolution Dean flow fractionation (HiDFF) technique developed by Tay et al.^{22,23} exploits differences in the minimum inner distances of particles under Dean force-dominated conditions to achieve high-resolution separation, and it has been successfully applied to the controlled release optimization of polydisperse drug-loaded particles and the

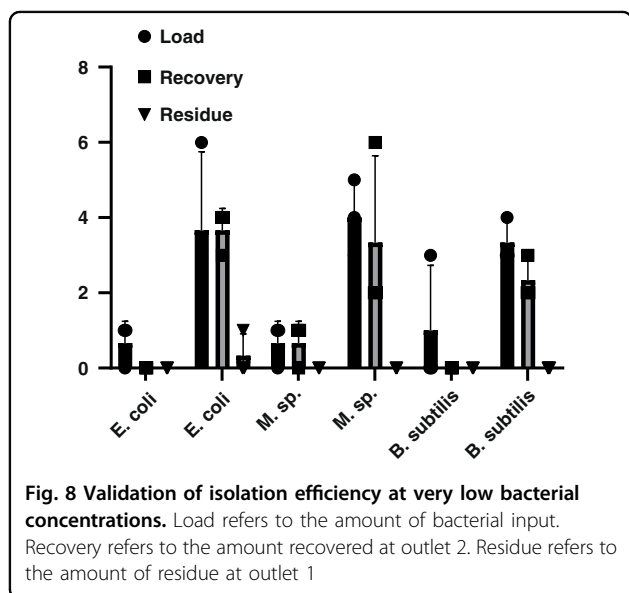


Table 1 Summary of microfluidic systems for particle and bioparticle separation

Bioparticles of interest	H (μm)	W (μm)	Flow rate ratio μl/min	Re	Beads (μm)	a_p/h	Separation efficiency(%)	Type of manipulation
Evs (20–200 nm) ²³	55	300	420 (1:20)	42	0.05–2	0.036	60	(i)
Mps (0.1–1 μm) ²²	55	300	660 1:10)	30–50	0.05–3	0.054	80	(i)
Beads (1.9 μm) ³⁴	50	100	20 (Null)	5	1.9&7.32	0.038	Null	(ii)
E.coli (<3 μm) ²⁰	80	500	1700 (3:31)	97.7	Null	0.038	>65	(ii)
E.coli (<3 μm) ²¹	20	50	78 (1:5)	37.14	0.81,2,29,4.7	0.045	98	(ii)
Platelets (2–3 μm) ³⁵	115	500	1430 (1:10)	77.5	Null	0.026	>80	(ii)
Nps (<5 μm) ³⁶	115	500	1320 (1:10)	71.5	2–5	0.043	>95	(ii)
S.aureus & E.coli (<3 μm) ³⁷	70	200	500 (1:4)	79.4	1.84,6,04,10.6	0.043	70.6–82.5	(ii)

(i) Low Reynolds number condition. (ii) Moderate Reynolds number condition
 Evs extracellular vesicles, Nps Nanoparticles, MVs Microvesicles, Null No data available

rapid sorting of microvesicles in blood. Notably, the particle migration pattern observed in HiDFF is highly consistent with the low Reynolds number regime proposed in our study. In Tay et al.'s experiments, a channel height of $h = 55\mu\text{m}$ resulted in $1\text{--}3\mu\text{m}$ particles undergoing Dean force-dominated lateral migration, corresponding to a characteristic length ratio of $a_p/h = 0.055$, which is very close to our proposed threshold of $a_p/h < 0.06$. Additionally, other studies with channel heights ranging from 20 to $115\mu\text{m}$, despite targeting different separation objectives^{20,21,34–37}, all conform to the principle of $a_p/h < 0.05$. This finding is highly consistent with our results under moderate Reynolds numbers, where particles with $a_p/h < 0.05$ are dominated by Dean force, although $a_p/h < 0.04$ is still recommended. Under moderate Reynolds conditions, particles with $a_p/h < 0.04$ are completely dominated by Dean force and exhibit high consistency in lateral position across the tested Reynolds number range, whereas particles with $0.04 < a_p/h < 0.05$, although predominantly influenced by Dean force, begin to experience inertial effects—resulting in significant differences in focusing behavior. As the Reynolds number increases further, the intensifying inertial influence eventually leads to noticeable deviations in lateral position compared to particles with $a_p/h < 0.04$. These results provide important experimental validation for microfluidic separation strategies based on the combined inertial-Dean flow effects and offer theoretical guidance for the design of efficient and precise small particle separation systems in the future.

The manufacture of cell therapies demands closed, automated systems that minimize contamination while ensuring consistent product quality. Although “GMP-in-a-box” platforms have automated upstream steps—cell sorting, activation, and expansion—critical quality-control (QC) operations (sampling, pretreatment, and microbial assays) remain offline and manual, extending turnaround times and introducing secondary-contamination risks^{6,7}. We propose a benchtop-validated microfluidic QC module that operates under continuous-flow conditions. Rather than a single 1 mL sample, the device continuously processes culture fluid, achieving $3\text{--}6\text{ mL/h}$ throughput; throughput can be further scaled by channel multiplexing or cascading. Driven by embedded peristaltic pumps and real-time flow sensors (Fig. S8), it passively separates contaminant-sized particles ($<5\mu\text{m}$) from therapeutic cells ($>6\mu\text{m}$) via combined inertial and Dean flows, then routes each fraction directly to downstream detectors without manual intervention. Benchtop testing at model loads (10^5 per mL bacteria; 10^6 cells/mL T cells) yielded $>95\%$ contaminant removal and $>96\%$ cell recovery with high purity and viability. Crucially, at clinically relevant microbial loads ($<100\text{ CFU/mL}$), the module consistently achieved 100% detection for inocula $\geq 1\text{ CFU/mL}$,

demonstrating sensitivity under low-load conditions. Inconsistent recovery at exactly 1 CFU/mL likely reflects inevitable sampling losses at the single-cell limit, underscoring the need for optimized sample volumes and enrichment protocols. Although still at the proof-of-concept stage, this continuous, closed-loop QC approach offers clear advantages over batch-style, offline testing: it reduces assay latency, eliminates sample transfers, and provides near real-time sterility feedback amenable to dynamic process control.

Future work will focus on integrating standardized GMP-compliant fluidic interfaces, validating long-term reliability, and coupling with inline molecular assays. When implemented within a “GMP-in-a-box” ecosystem, this module could transform QC from a discrete bottleneck into an automated, scalable component of next-generation cell therapy manufacturing.

Acknowledgements

This research was supported by the National Medical Products Administration [Grant No. GZYZY2023001], and the Chinese Academy of Engineering [Grant No. 2024WK1006], and The National Natural Science Foundation of China–Youth Science Fund [Grant No. 82204538]. The authors appreciate the support from the Tianjin University School of Medicine for this study. We also appreciate the support provided by the Hangzhou Institute of Medicine (HIM), Chinese Academy of Sciences. Special thanks are extended to the Scientific Experimental Center (Flow Cytometry (Jie Deng) and Microscopy Imaging Facility (Anqi Qin)) of the HIM, for their technical assistance. We express our gratitude to the research group of Liang Dong and Zhao Pan at the HIM for their valuable assistance. The authors are particularly grateful to the research group led by Prof. Jinzhao Song at the HIM for their valuable contributions. Finally, we thank all researchers in the Laboratory of Cell Therapy Technology, HIM, for their contributions to this study.

Author contributions

J.H.T. and J.J.H. proposed the research idea. J.H.T. and M.Z. designed the particle experiments. J.B.Y. and L.P.Z. participated in the design of the biological experiments, including cells and bacteria. J.H.T. carried out the experiments. Z.M.H., J.H.T., and W.Z.Y. analyzed the data. L.X. and C.S.S. provided technical support. J.H.T., M.Z., and L.P.Z. compiled the paper, and all authors participated in the paper. The paper was reviewed by all authors.

Conflict of interest

The authors declare no competing interests.

Supplementary information The online version contains supplementary material available at <https://doi.org/10.1038/s41378-025-01043-w>.

Received: 31 March 2025 Revised: 17 July 2025 Accepted: 4 August 2025
Published online: 26 January 2026

References

- Nardo, D., Maddox, E. G. & Riley, J. L. Cell therapies for viral diseases: a new frontier. *Semin. Immunopathol.* **47**, 1–10 (2025).
- Schett, G., Mackensen, A. & Mougiakakos, D. CAR T-cell therapy in autoimmune diseases. *Lancet* **402**, 2034–2044 (2023).
- Gebo, J. E. T. & Lau, A. F. Sterility testing for cellular therapies: what is the role of the clinical microbiology laboratory?. *J. Clin. Microbiol.* **58**, e01492–19 (2020).
- Li, Y., Huo, Y., Yu, L. & Wang, J. Z. Quality control and nonclinical research on CAR-T cell products: general principles and key issues. *Engineering* **5**, 122–131 (2019).

5. European Directorate for the Quality of Medicines & HealthCare (EDQM). European Pharmacopoeia (12th Edition). European Directorate for the Quality of Medicines & HealthCare, <https://www.edqm.eu/en/european-pharmacopoeia>.
6. U.S. Food and Drug Administration. Chemistry, manufacturing, and control (CMC) information for human gene therapy investigational new drug applications (INDs). U.S. Food and Drug Administration, <https://www.fda.gov/media/113760/download>.
7. England, M. R., Stock, F., Gebo, J. E. T., Frank, K. M. & Lau, A. F. Comprehensive evaluation of compendial USP<71>, BacT/Alert Dual-T, and Bactec FX for detection of product sterility testing contaminants. *J. Clin. Microbiol.* **57**, e01548–18 (2019).
8. Surrette, C. et al. Rapid microbiology screening in pharmaceutical workflows. *SLAS Technol.* **23**, 387–394 (2018).
9. Xing, G., Zhang, W., Li, N., Pu, Q. & Lin, J.-M. Recent progress on microfluidic biosensors for rapid detection of pathogenic bacteria. *Chin. Chem. Lett.* **33**, 1943–1958 (2022).
10. Jiang, M., Severson, K. A. & Love, J. C. Opportunities and challenges of real-time release testing in biopharmaceutical manufacturing. *Biotechnol. Bioeng.* **114**, 2445–2456 (2017).
11. Ceja, M. A., Khericha, M., Harris, C. M., Puig-Saus, C. & Chen, Y. Y. CART cell manufacturing: major process parameters and next-generation strategies. *J. Exp. Med.* **221**, e20230903 (2024).
12. Di Carlo, D. Inertial microfluidics. *Lab Chip* **9**, 3038–3046 (2009).
13. Xiang, N. et al. Improved understanding of particle migration modes in spiral inertial microfluidic devices. *RSC Adv.* **5**, 77264–77273 (2015).
14. Zhang, J., Li, W. & Alici, G. Inertial microfluidics: mechanisms and applications. In: Zhang, D. & Wei, B. (eds.) *Advances in mechatronics and MEMS devices II*, 563–593 (Springer, 2017).
15. Mehran, A. et al. High-throughput, label-free isolation of white blood cells from whole blood using parallel spiral microchannels with u-shaped cross-section. *Biosensors* **11**, 406 (2021).
16. Shirai, K. et al. Hybrid double-spiral microfluidic chip for RBC-lysis-free enrichment of rare cells from whole blood. *Lab Chip* **22**, 4418–4429 (2022).
17. Bhagat, A. A. S., Kuntaegowdanahalli, S. S. & Papautsky, I. Inertial microfluidics for continuous particle filtration and extraction. *Microfluid. Nanofluid.* **7**, 217–226 (2009).
18. Kuntaegowdanahalli, S. S., Bhagat, A. A. S., Kumar, G. & Papautsky, I. Inertial microfluidics for continuous particle separation in spiral microchannels. *Lab Chip* **9**, 2973–2980 (2009).
19. Hou, H. W. et al. Isolation and retrieval of circulating tumor cells using centrifugal forces. *Sci. Rep.* **3**, 1259 (2013).
20. Hou, H. W., Bhattacharyya, R. P., Hung, D. T. & Han, J. Direct detection and drug-resistance profiling of bacteremias using inertial microfluidics. *Lab Chip* **15**, 2297–2307 (2015).
21. Lee, J.-H., Lee, S.-K., Kim, J.-H. & Park, J.-H. Separation of particles with bacterial size range using the control of sheath flow ratio in spiral microfluidic channel. *Sens. Actuators A Phys.* **286**, 211–219 (2019).
22. Tay, H. M. et al. Rapid purification of sub-micrometer particles for enhanced drug release and microvesicles isolation. *NPG Asia Mater.* **9**, e434 (2017).
23. Tay, H. M. et al. Direct isolation of circulating extracellular vesicles from blood for vascular risk profiling in type 2 diabetes mellitus. *Lab Chip* **21**, 2511–2523 (2021).
24. Zhang, B., Zhao, W., Wang, Z., Zhao, Q. & Wu, W. Assistance of inertial microfluidics in membrane-based microfiltration. *J. Water Process. Eng.* **53**, 103762 (2023).
25. Zhang, B., Zhao, W., Yuan, D., Wang, T. & Wu, W. A novel microparticle size sorting technology based on sheath flow stable expansion regimes. *Phys. Fluids* **35**, 052018 (2023).
26. Johnston, I. D. et al. Dean flow focusing and separation of small microspheres within a narrow size range. *Microfluid. Nanofluid.* **17**, 509–518 (2014).
27. Dean, W. R. Stream-line motion of fluid in a curved pipe (second paper). *Philos. Mag.* **5**, 673–695 (1928).
28. Di Carlo, D., Irimia, D., Tompkins, R. G. & Toner, M. Continuous inertial focusing, ordering, and separation of particles in microchannels. *Proc. Natl. Acad. Sci. USA* **104**, 18892–18897 (2007).
29. Asmolov, E. S. Inertial lift on a spherical particle in a plane Poiseuille flow at large channel Reynolds number. *J. Fluid Mech.* **381**, 63–87 (1999).
30. Liu, C., Hu, G., Jiang, X. & Sun, J. Inertial focusing of spherical particles in rectangular microchannels over a wide range of Reynolds numbers. *Lab Chip* **15**, 1168–1177 (2015).
31. Bhagat, A. A. S., Kuntaegowdanahalli, S. S. & Papautsky, I. Enhanced particle filtration in straight microchannels using shear-modulated inertial migration. *Phys. Fluids* **20**, 101702 (2008).
32. Ookawara, S., Higashi, R., Street, D. & Ogawa, K. Feasibility study on concentration of slurry and classification of contained particles by microchannel. *Chem. Eng. J.* **101**, 171–178 (2004).
33. Ookawara, S., Street, D. & Ogawa, K. Numerical study on development of particle concentration profiles in a curved microchannel. *Chem. Eng. Sci.* **61**, 3714–3724 (2006).
34. Bhagat, A. A. S., Kuntaegowdanahalli, S. S. & Papautsky, I. Continuous particle separation in spiral microchannels using Dean flows and differential migration. *Lab Chip* **8**, 1906–1912 (2008).
35. Tay, H. M. et al. Multiplexed label-free fractionation of peripheral blood mononuclear cells for identification of monocyte-platelet aggregates. *Anal. Chem.* **90**, 14535–14542 (2018).
36. Yeo, D. C. et al. Interference-free micro/nanoparticle cell engineering by use of high-throughput microfluidic separation. *ACS Appl. Mater. Interfaces* **7**, 20855–20864 (2015).
37. Esan, A., Vanholsbeeck, F., Swift, S. & McGoverin, C. M. Continuous separation of bacterial cells from large debris using a spiral microfluidic device. *Biomicrofluidics* **17**, 044104 (2023).